

Article

Surfactant-Capped Silver-Doped Calcium Oxide Nanocomposite: Efficient Sorbents for Rapid Lithium Uptake and Recovery from Aqueous Media

Urooj Kamran ^{1,*}, Hasan Jamal ², Md Irfanul Haque Siddiqui ³  and Soo-Jin Park ^{4,*}

¹ Institute of Advanced Machinery Design Technology, Korea University, 145 Anam-ro, Seongbuk-gu, Seoul 02841, Republic of Korea

² Division of Energy Technology, Daegu Gyeongbuk Institute of Science & Technology, 333, Techno Jungang-Daero, Hyeonpung-Myeon, Dalseong-Gun, Daegu 42988, Republic of Korea

³ Department of Mechanical Engineering, King Saud University, Riyadh 11451, Saudi Arabia

⁴ Department of Chemistry, Inha University, 100 Inharo, Incheon 22212, Republic of Korea

* Correspondence: malikurooj9@gmail.com (U.K.); sjpark@inha.ac.kr (S.-J.P.)

Abstract: The demand for lithium is constantly increasing due to its wide range of uses in an excessive number of industrial applications. Typically, expensive lithium-based chemicals (LiOH, LiCl, LiNO₃, etc.) have been used to fabricate adsorbents (i.e., lithium manganese oxide) for lithium ion (Li⁺) adsorption from aqueous sources. This type of lithium-based adsorbent does not seem to be very effective in recovering Li⁺ from water from an economic point of view. In this study, an innovative nanocomposite for Li⁺ adsorption was investigated for the first time, which eliminates the use of lithium-based chemicals for preparation. Here, calcium oxide nanoparticles (CaO-NPs), silver-doped CaO nanoparticles (Ag-CaO-NPs), and surfactant (polyvinylpyrrolidone (PVP) and sodium dodecyl sulfate (SDS))-modified Ag-CaO (PVP@Ag-CaO and SDS@Ag-CaO) nanocomposites were designed by the chemical co-precipitation method. The PVP and SDS surfactants acted as stabilizing and capping agents to enhance the Li⁺ adsorption and recovery performance. The physicochemical properties of the designed samples (morphology, size, surface functionality, and crystallinity) were also investigated. Under optimized pH (10), contact time (8 h), and initial Li⁺ concentration (2 mg L⁻¹), the highest Li⁺ adsorption efficiencies recorded by SDS@Ag-CaO and PVP@Ag-CaO were 3.28 mg/g and 2.99 mg/g, respectively. The nature of the Li⁺ adsorption process was examined by non-linear kinetic and isothermal studies, which revealed that the experimental data were best fit by the pseudo-first-order and Langmuir models. Furthermore, it was observed that the SDS@Ag-CaO nanocomposite exhibited the highest Li⁺ recovery potential (91%) compared to PVP@Ag-CaO (85%), Ag-CaO NPs (61%), and CaO NPs (43%), which demonstrates their regeneration potential. Therefore, this type of innovative adsorbents can provide new insights for the development of surfactant-capped nanocomposites for enhanced Li⁺ metal recovery from wastewater.

Keywords: transition metal doping; lithium; stabilizer; nanocomposites; metal recovery; adsorption



Citation: Kamran, U.; Jamal, H.; Siddiqui, M.I.H.; Park, S.-J. Surfactant-Capped Silver-Doped Calcium Oxide Nanocomposite: Efficient Sorbents for Rapid Lithium Uptake and Recovery from Aqueous Media. *Water* **2023**, *15*, 3368. <https://doi.org/10.3390/w15193368>

Academic Editor: Alessandro Erto

Received: 4 August 2023

Revised: 20 September 2023

Accepted: 21 September 2023

Published: 25 September 2023



Copyright: © 2023 by the authors. Licensee MDPI, Basel, Switzerland. This article is an open access article distributed under the terms and conditions of the Creative Commons Attribution (CC BY) license (<https://creativecommons.org/licenses/by/4.0/>).

1. Introduction

Lithium (Li) has become an indispensable element in recent decades due to its efficient electrochemical activity and excellent heat capacity because of the current industrial revolution [1–3]. Its applications include lithium ion batteries, ceramics, lubricants, catalysts, etc. [4,5]. Remarkably, in the last five years, the use of batteries for electric vehicles and other electronic devices has been tremendously boosted by the policy of substituting conventional fuel energy with blue renewable energy in most countries [6–8]. The increase in global Li consumption over the last 12 years is challenging the supply of Li from conventional ore sources. Considering that Li recovery from aqueous media has tremendous merits as a substitute Li source, as about 75% of Li ions (Li⁺) are deposited in

geo-thermal brines and salt lakes in several countries [9], as well as within the ocean, the Li^+ is deposited an over sixteen-thousand order or a magnitude higher compared to that on Earth's surface [10]. Seawater is considered a prospective aqueous source of Li^+ ions to fully meet the increasing global demand for Li for industrialization [11].

To recover or extract lithium from different aqueous sources, several conventional technologies have been used, such as chemical precipitation [12], solvent extraction [13], ion exchange [14], nanofiltration [15], membrane technology [16], adsorption [17–19], reaction-coupled separation [20], etc. Among these investigated technologies for Li^+ recovery, adsorption seems to be a very ideal method from an economic viewpoint and in terms of environmental friendliness [21,22]. Adsorption has overwhelming advantages such as less energy consumption, easy handling, fast operation, versatility, and less expense. Using the adsorption method, several materials have been developed to recover lithium from aqueous media, such as lithium ion sieves, including HMnO [23], $\text{H}_{1.6}\text{Mn}_{1.6}\text{O}_4$ ion sieves [24], and metal-doped $\text{Li}_{1.6}\text{Mn}_{1.6}\text{O}_4$ [25]. The disadvantages of using these materials include the need for high energy consumption with an excessive number of synthetic steps during the fabrication process, the requirement for a large number of Li-based precursors (e.g., lithium hydroxide, lithium chloride, and lithium nitrate), low chemical stability during Li^+ adsorption–desorption experiments, and expensive design [26]. These circumstances encourage the breakthrough of an alternative by eliminating the use of expensive Li-based chemicals and reducing the number of complex synthesis steps to design innovative materials for efficient and rapid Li^+ recovery from aqueous sources.

Recently, alkaline earth metal oxides are of great interest to researchers and have been widely used for various applications. For example: (i) magnesium oxide nanoparticles have been used for dye removal from wastewater and tissue culture applications [27,28]; (ii) barium oxide nanoparticles have been used for dye photodegradation [29]; (iii) calcium oxide nanoparticles have been used for pollutant removal [30,31], carbon dioxide adsorption [32], catalysis [33], and antimicrobial applications [34]. Among these metal oxide nanoparticles, the oxides of calcium (CaO) have been dominantly used in various applications due to their efficient physicochemical properties. It has been observed that the performance of CaO is improved by doping it with different materials and transition metals (e.g., Ag, Ni, etc.) [35,36]. This is because the introduction of dopants creates new states in the oxide gap, which improves its performance. Furthermore, efforts have been made to stabilize nanoparticles by using capping agents, which seem to be very effective in reducing the aggregation of doped nanoparticles and improving their dispersion stability in aqueous media [37]. The well-known capping agents and stabilizers are considered surfactants. From the literature, it has been observed that the stabilization of nanomaterials with the polyvinylpyrrolidone (PVP) surfactant resulted in the improvement of PVP-coated nanocomposites' performance with enhanced adsorption of metals and dyes from water [38,39]. In addition, sodium-dodecyl-sulfate (SDS)-stabilized iron nanoparticles resulted in the increase of chromium ion removal potential from wastewater [40]. Besides, other reported literature in terms of stabilized nanoparticles showed that polyvinyl-alcohol-stabilized nanofibers [41], cetyltrimethylammonium-bromide-stabilized magnetic nanoparticles [42], and polyethylene-glycol-stabilized bimetallic nanoparticles [43] also seemed to be efficient for improving the adsorption performance. Among them, the PVP and SDS surfactants can serve as unique stabilizers, because the PVP stabilizer acts as an effective reducing agent depending on the specific manufacturing conditions [44] and SDS acts as an excellent nanoparticle dispersant [45]. It has been shown that the PVP surfactant prevents nanoparticles from self-aggregating through repulsive forces generated by its lyophobic carbon chain, which spread throughout the solvent and interact with each other [46]. Therefore, considering the above aspects, the development of PVP- and SDS-stabilized Ag-doped CaO nanocomposites specifically for rapid Li^+ adsorption and recovery has not yet been reported.

The focus of this research was based on the design of CaO-NPs, Ag-doped CaO, and PVP- and SDS-stabilized Ag-CaO as nanocomposites by a simple chemical co-precipitation

method. The crystallographic, morphological, and surface functional properties of the prepared samples were evaluated. The batch adsorption experiment was carried out to determine the Li^+ adsorption potential at different pH by using such a kind of stabilized CaO-based nanocomposites for the first time. In addition, the desorption experiment was carried out to determine the Li^+ recovery of the samples from an aqueous source by using a desorbing agent.

2. Materials and Experimental Protocols

2.1. Materials

Calcium chloride dihydrate ($\text{CaCl}_2 \cdot 2\text{H}_2\text{O}$) of $\geq 99\%$ purity was purchased from Duskan Pure Chemical Co-Ltd., Seoul, Republic of Korea. Surfactants (acting as capping agents and surface stabilizers) including PVP with an average molecular weight of 40,000 g/mol and SDS of $\geq 99.0\%$ purity were ordered from Sigma Aldrich, Burlington, MA, USA. Chemicals such as silver nitrate (AgNO_3) of $\geq 99.0\%$ purity, hydrochloric acid (HCl) of 60% purity, ethanol, and sodium hydroxide (NaOH) of $\geq 98\%$ purity were purchased from Dae-Jung, Republic of Korea. The lithium solution as an atomic absorption standard at a concentration of 1000 mg/L was ordered from Standard, USA. All these chemicals were used without any further purification, and all were of analytical grade. During all experiments, distilled water (DW) was utilized.

2.2. Synthesis of Pristine CaO Nanoparticles

To prepare pristine CaO nanoparticles, several steps were followed as briefly mentioned in Figure 1a. The 0.5 M NaOH of approximately 100 mL was added dropwise to the $\text{CaCl}_2 \cdot 2\text{H}_2\text{O}$ solution of 0.25 M (with a volume of 150 mL). The mixture was stirred for 40 min at room temperature, and white precipitates formed. The white precipitates were then separated by vacuum filtration followed by washing with DW. After oven drying, the white powder was calcined in an air atmosphere at 350°C for 3 h [47]. The obtained CaO nanoparticles are referred to as CaO-NPs.

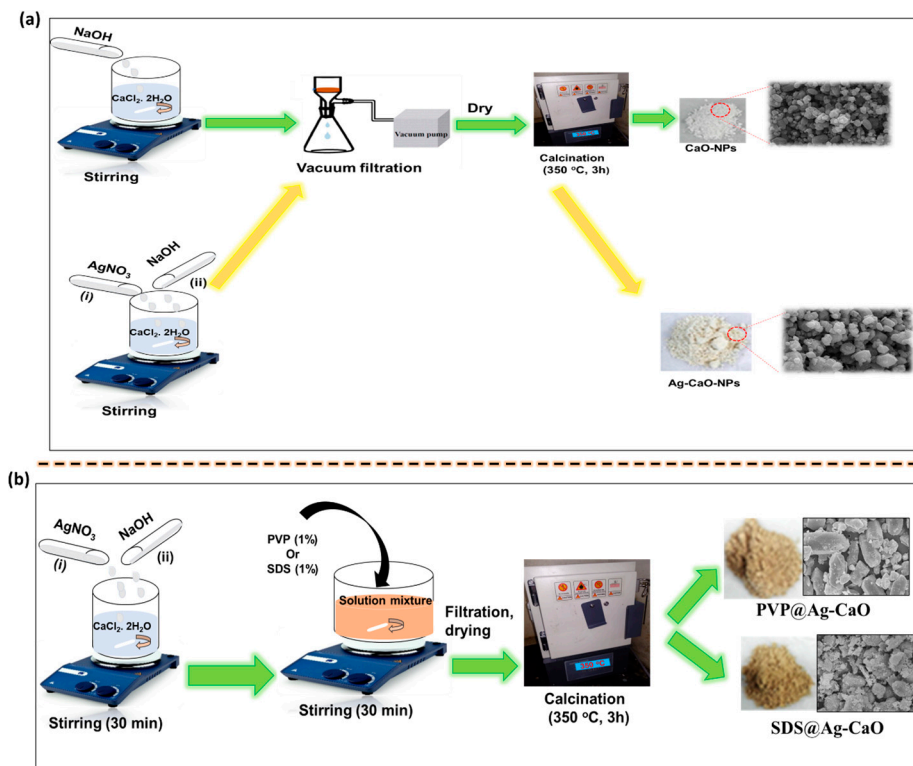


Figure 1. Schematic illustration for the fabrication of (a) CaO-NPs and Ag-CaO-NPs and (b) PVP@Ag-CaO and SDS@Ag-CaO nanocomposites.

2.3. Synthesis of Ag-Doped CaO and Surfactant-Capped Ag-CaO Nanocomposites

The fabrication of silver-doped CaO NPs, as shown in Figure 1a, involved several steps: First, 3.675 g of $\text{CaCl}_2 \cdot 2\text{H}_2\text{O}$ was dissolved in 100 mL of DW to obtain a concentration of 0.25 M, then 10 mL of AgNO_3 (0.3 mM) was added dropwise under constant stirring. The solution mixture was stirred for 30 min at room temperature. Then, the 0.5 M NaOH solution was added dropwise and stirred for 1 h. The prepared Ag-CaO nanoparticles were filtered through Whatman filter paper (0.45 μm) followed by rinsing with a solution mixture of DW and ethanol (1:1). After drying at 100 °C for 5 h, the obtained dried powder was calcined at 350 °C for 3 h to produce Ag-CaO nanoparticles (Ag-CaO NPs) [48].

The schematic layout for the fabrication of PVP-capped Ag-CaO and SDS-capped Ag-CaO nanocomposites is shown in Figure 1b. After dropwise addition of NaOH and AgNO_3 in $\text{CaCl}_2 \cdot 2\text{H}_2\text{O}$, the 1% of PVP and SDS were added individually in a volume of 100 mL and stirred for another 30 min. After vacuum filtration, the samples were washed with DW:ethanol and dried. The obtained powdered samples were calcined at 350 °C for 3 h [49]. The nanocomposites prepared by using PVP and SDS are designated as PVP@Ag-CaO and SDS@Ag-CaO nanocomposites, respectively.

2.4. Batch Adsorption Experiment

A batch adsorption experiment was carried out to determine the Li^+ adsorption potential of the designed samples. The experiments were carried out at different pH ranges between 2 and 10 by adding a 0.1 g material dosage at ambient temperature by maintaining the Li^+ concentration up to 2 ppm of a 150 mL volume. The solution mixture was stirred at a shaking speed of 230 rpm for 5 h to reach equilibrium. After reaching equilibrium, the filtrate was analyzed using an atomic absorption spectrometer (PerkinElmer, Analyst 400, USA) to evaluate the residual concentration of Li^+ in the aqueous media. The removal efficiency of Li^+ and the adsorption potential at equilibrium were calculated using Equations (1) and (2) [50,51]:

$$\text{Removal efficiency (RE) (\%)} = \frac{C_o - C_e}{C_o} \times 100 \quad (1)$$

$$q_e = (C_o - C_e) \frac{V}{W} \quad (2)$$

where q_e is the adsorption capacity at equilibrium (q_e) or at a certain time (q_t) and is measured in mg/g. C_o and C_e are the primary and equilibrium concentrations of Li^+ in the aqueous sources, respectively, and are measured in ppm or mg L^{-1} . “V” is the volume in liters (“L”), and “W” is the weight of the sample and recorded in grams (“g”).

2.5. Li^+ Recovery by Desorption

The Li^+ -loaded samples of the CaO-NPs, Ag-CaO-NPs, PVP@Ag-CaO, and SDS@Ag-CaO nanocomposites obtained by filtration were dried at 60 °C in an oven. The dried samples were dispersed in 150 mL of HCl solutions of different concentrations (0.05, 0.5, and 1 M) and allowed to stir at 230 rpm by a magnetic stirrer for 6 h. After filtration, the obtained filtrate was measured by AAS to investigate the concentration of the Li^+ recovered in an aqueous source. The Li^+ desorption efficiency of the prepared samples was calculated using Equation (3) [52]:

$$\text{Desorption (\%)} = \frac{C_{des.}}{C_o} \times 100 \quad (3)$$

where C_{des} (mg L^{-1}) represents the desorbed or recovered concentration of Li^+ ions within the aqueous source after the desorption experiment. C_o is the initial Li^+ concentration in mg L^{-1} that was adsorbed.

2.6. Characterizations

The samples were characterized using a variety of instruments to determine their physicochemical properties. The morphology and size of the samples were analyzed by scanning electron microscopy (SEM) (Model SU8010, Hitachi Co., Ltd., Tokyo, Japan) and transmission electron microscopy (TEM) (Philips; CM200). The crystalline nature of the nanoparticles and nanocomposites was determined by X-ray diffraction (XRD) using a D2 PHASER (BRUKER, Billerica, MA, USA). The XRD peaks were recorded between angles of 10° and 80°. The surface functional groups present above the surface of the nanoparticles and nanocomposites were determined by Fourier transform infrared spectroscopy (FTIR) (Jasco PS-4000). In addition, the Li⁺ ion concentration within the aqueous source before and after the experiments was analyzed by an atomic absorption spectrometer (AAS) (Perkinelmer, Analyst 400, Waltham, MA, USA).

3. Results and Discussion

3.1. Structural and Morphological Examination (SEM and TEM)

The surface morphology of the prepared samples of the CaO-NPs, Ag-CaO-NPs, PVP@Ag-CaO, and SDS@Ag-CaO nanocomposites was examined by SEM at 5 μm magnification. As shown in Figure 2a,b, the crystals of CaO-NPs and Ag-CaO-NPs had an irregular morphology and show the aggregation of nanoparticles in the absence of any stabilizing or capping agent. The agglomeration of nanoparticles (Figure 2a,b) showed the porous nature of the particles. The SEM micrographs of the nanocomposites (Figure 2c,d) showed a tremendous decrease in the agglomeration ratio due to the stabilization by the capping agents PVP and SDS. These results are in agreement with the previously reported literature, where the prevention of the agglomeration of zinc sulfide nanoparticles was carried out by using similar types of stabilizing agents (PVP and SDS) as the surfactants [53]. The SEM image of the PVP@Ag-CaO nanocomposite showed the cylinder-like morphology with sharp edges, as mentioned in Figure 2c. Some cylindrical crystals were small, while some were large. Furthermore, the SDS@Ag-CaO nanocomposite showed irregularly structured blocks with a smaller aggregation ratio, as mentioned in Figure 2d. Typically, the surface functionalities of the surfactants used provided a physical barrier between the adjacent CaO-NPs and resulted in the highly stabilized structure of the nanocomposites, as shown in Figure 2c,d. This concept was discussed in the previously reported work [54]. By considering the stability of the designed materials in terms of hygroscopicity, it is clearly shown by the SEM images of the samples (CaO-NPs, Ag-CaO-NPs, PVP@Ag-CaO, and SDS@Ag-CaO) how well their original appearance and quality were maintained despite their exposure to moisture or humidity. The high stability of the hygroscopicity implies that the samples remained relatively unchanged in their moisture-absorbing behavior and appearance.

The size of the samples was also investigated by TEM analysis. The CaO NPs and Ag-CaO NPs showed that the particles were aggregated (larger than 100 nm in size and recorded between 200 nm and 500 nm) with a spherical and square-type morphology, as mentioned in Figure 3a–d. However, the PVP@Ag-CaO and SDS@Ag-CaO nanocomposites had smaller particle sizes recorded at 50 nm and 100 nm, shown in Figure 3e–h. It is evident that PVP and SDS also played an important role in reducing the size of the nanocomposites, as well as improving the dispersion of the nanoparticles. It was found that the Ag-CaO nanoparticles were capped and stabilized by the capping agents (PVP and SDS) together with silver doping. Therefore, the uniform distribution, low aggregation rate, and size reduction were achieved by using the capping agents [55].

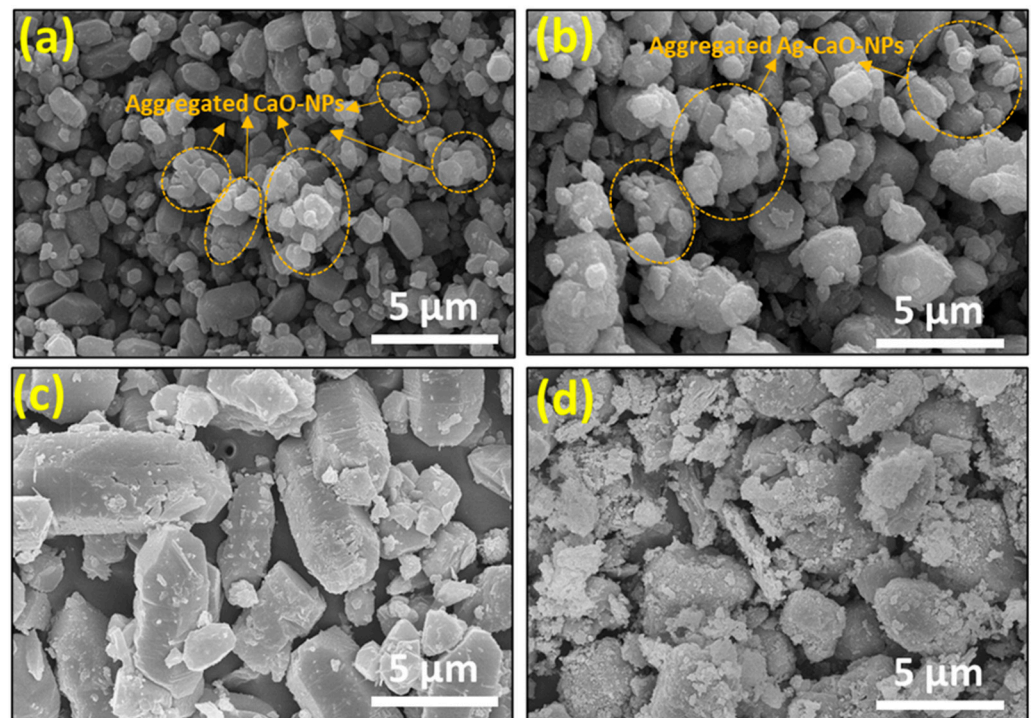


Figure 2. SEM micrographs of (a) CaO-NPs, (b) Ag-CaO-NPs, (c) PVP@Ag-CaO, and (d) SDS@Ag-CaO.

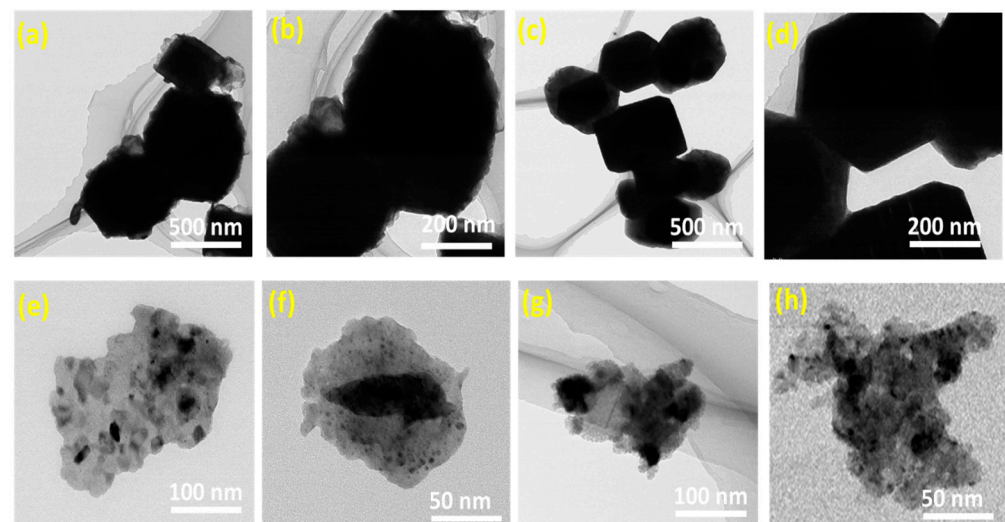


Figure 3. HR-TEM images of (a,b) CaO-NPs, (c,d) Ag-CaO-NPs, (e,f) PVP@Ag-CaO, and (g,h) SDS@Ag-CaO attained at different resolutions.

3.2. Crystalline Structure or Crystallographic Analysis

The XRD patterns of the prepared materials were obtained at two theta angles ranging from 10° – 80° , as shown in Figure 4a. The XRD pattern of the CaO-NPs showed peaks at 28.65° , 34.01° , 44.16° , 54.41° , and 64.24° corresponding to the (011), (111), (012), (022), and (311) crystallographic planes of the cubic network of the face-centered lattice CaO-NPs. The peaks positioned at 18.09° , 50.82° , and 62.63° corresponded to $\text{Ca}(\text{OH})_2$ on the basis of Map No. 04-007-5231 [56]. The XRD pattern of the Ag-CaO-NPs showed the increase in the peak intensities, indicating that the Ag doping successfully increased the crystallinity of the CaO-NPs. The observed peaks at 31.87° , 38.22° , and 45.55° were characteristic of peaks with phase plane (111) of the face-centered cubic phase of metallic Ag [57]. The XRD pattern of the PVP@Ag-CaO and SDS@Ag-CaO nanocomposite showed a slight decrease in all peak intensities, which evidenced that the Ag-CaO NPs were capped and stabilized by

the PVP and SDS capping agents. The semi-crystalline nature of the nanocomposites was also demonstrated.

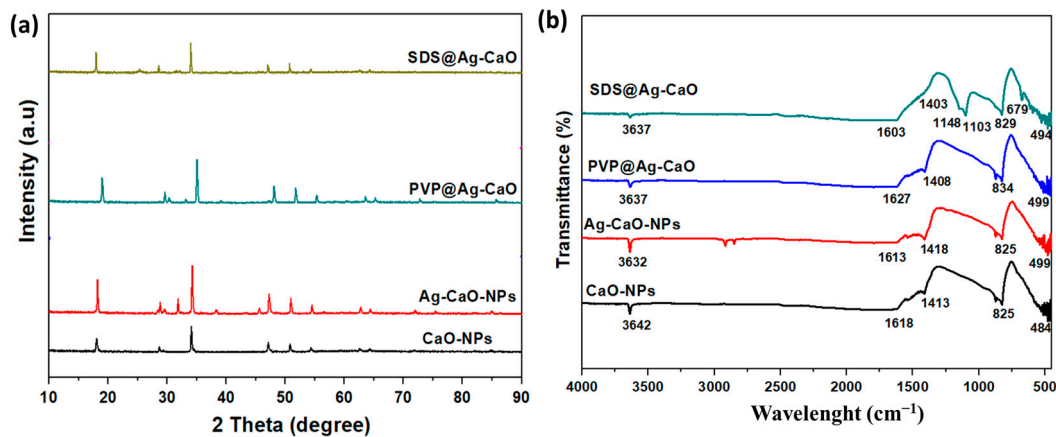


Figure 4. (a) XRD pattern of CaO-NPs, Ag-CaO-NPs, PVP@Ag-CaO, and SDS@Ag-CaO and (b) FTIR spectra of CaO-NPs, Ag-CaO-NPs, PVP@Ag-CaO, and SDS@Ag-CaO nanocomposites.

3.3. Surface Functional Analysis

To investigate the surface functional properties of the nanoparticles and nanocomposites, the FTIR spectra were recorded in the range of 500 to 4000 cm⁻¹, as shown in Figure 4b. The peaks located at 3642 cm⁻¹, 3632 cm⁻¹, and 3637 cm⁻¹ of the CaO-NPs, Ag-CaO-NPs, and nanocomposite corresponded to the hydroxyl group (O-H stretching vibrations) due to the absorption of water molecules in the samples (Figure 4b). The peaks recorded in the region between 1403 and 1418 cm⁻¹ and within 825–834 cm⁻¹ showed the C-O linkage, which occurred due to the carbonization of the CaO-NPs [58]. During the calcination process, the exposure of the highly active surface of the CaO-NPs to air resulted in the generation of CO₂ and water molecules, which were further sorbed above the nanoparticle surface in the form of free hydroxyl and carbonate moieties. The hygroscopic properties of incense-stick-ash (ISA)-derived CaO were determined in the light of previously reported recent literature [59]. In this reported work, the FTIR spectrum of ISA-derived CaO samples showed a small peak around 3400 cm⁻¹ corresponding to –OH stretching, and the peaks located in the region of 2200–2400 cm⁻¹ were occurred due to the adsorption of atmospheric moisture, as well as CO₂, leading to the formation of Ca(OH)₂. These results revealed the extremely hygroscopic nature of CaO, as it absorbs water content very rapidly. In addition to hygroscopicity, the point defects in most simple oxides have previously been analyzed and should be considered [60]. This is because the point defects present both in the bulk and on the surface of CaO strongly determine the surface functionalities of CaO. Furthermore, Chen and co-workers recently studied the non-equilibrium phase transition properties of alkali metal salt above the surface of CaO and analyzed the influence of the surface properties of CaO and the heating rate on the phase transition [61]. In this study, it was shown that surface defects within CaO effectively enhanced the interaction between CaO and the alkali metal salt. This was due to the surface of CaO becoming charged.

Moving forward, as mentioned in Figure 4b, the small shoulder located between 1603 and 1627 cm⁻¹ in all samples corresponded to the C-O stretch of the CO₂ stretching [62]. The vibrational peaks located in the range of 482–494 cm⁻¹ within the samples represented the confirmation of the main CaO vibrations, thus confirming the formation of CaO NPs [63]. Therefore, it can be concluded that the FTIR analysis indicated the traces of chemicals used in the preparation of the CaO nanoparticles. Compared to the CaO-NPs, the shift of the peak positions within the Ag-CaO-NPs and nanocomposites (PVP@Ag-CaO and SDS@Ag-CaO) indicated that the surface modification in terms of stabilization was successfully carried out. Within the FTIR spectrum of the SDS@Ag-CaO nanocomposite, the peaks positioned at 1148 cm⁻¹ and 1103 cm⁻¹ were attributed to S-O stretching and the bending

vibration of the SDS. These facts revealed the successful stabilization of the SDS molecules over the CaO NPs [64].

3.4. Li^+ Batch Adsorption Experiment

3.4.1. Effect of pH on Li^+ Adsorption Performance

The solvent pH plays an essential role in influencing the adsorption efficiency of the samples, as it affects the surface charge, the functional binding sites for sorption, and the interactions between the sorbate and the material surface [65]. Therefore, it seems very important to investigate the effect of pH on the Li^+ uptake performance of the designed nanoparticles and nanocomposites. The batch adsorption experiment was performed by adjusting the pH of the Li^+ solution (2 ppm) from 2 to 10 using 0.1 M NaOH and 0.1 M HCl, and 0.1 g of the samples was added and stirred at 230 rpm for 4 h. The remaining Li^+ concentration in the aqueous solution after Li^+ adsorption was analyzed by AAS. The experimental results obtained are summarized in Figure 5a,b. In the acidic pH range, the Li^+ adsorption potential was very low together with the adsorption removal values between 1.4 and 5.0%, 6.8 and 13.5%, 11.1 and 30.15%, and 9.2 and 25.5% for the CaO-NPs, Ag-CaO-NPs, PVP@Ag-CaO, and SDS@Ag-CaO nanocomposites, respectively (as shown in Figure 5a). This occurred because, under an acidic pH, the surface of the adsorbent became positively charged due to excessive number of H^+ ions in the aqueous medium, which decreased the Li^+ adsorption potential. On the other hand, by increasing the pH (basic) of the Li^+ solution, the Li^+ adsorption of the CaO-NPs, Ag-CaO-NPs, PVP@Ag-CaO, and SDS@Ag-CaO nanocomposites was successively increased with adsorption percentages of 20.7%, 38.9%, 65.3%, and 57.1%, respectively. The reason may be that, at a higher pH, the adsorbent surface became more negatively charged and attracted the positively charged Li^+ ions from the aqueous source.

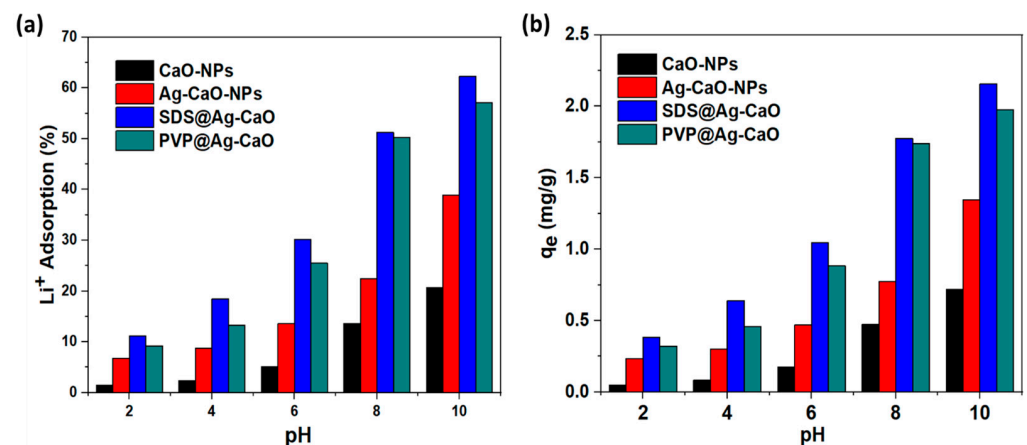


Figure 5. (a) Li^+ adsorption percentage of CaO-NPs, Ag-CaO-NPs, PVP@Ag-CaO, and SDS@Ag-CaO nanocomposites at different pH and (b) Li^+ adsorption potential of CaO-NPs, Ag-CaO-NPs, PVP@Ag-CaO, and SDS@Ag-CaO nanocomposites at different pH ranges.

The maximum recorded Li^+ adsorption capacity with the q_e values as mentioned in Figure 5b was 0.72 mg/g, 1.34 mg/g, 2.15 mg/g, and 1.97 mg/g for the CaO-NPs, Ag-CaO-NPs, PVP@Ag-CaO, and SDS@Ag-CaO nanocomposites, respectively. The highest Li^+ adsorption potential was recorded at pH 10 for the SDS@Ag-CaO nanocomposites compared to PVP@Ag-CaO, which may be due to several reasons: (i) the anionic nature of SDS (anionic surfactant), whereas PVP is a non-ionic surfactant, and (ii) the presence of a very strong negatively charged sulfonate group in SDS, which is not present in the PVP surfactant [66]. Zheng et al. [67] reported a similar type of pH effect trend by using the designed lanthanide-doped ion sieves. In that work, it was recorded that, by increasing the Li^+ solution pH from 2 to 10, the Li^+ adsorption potential of the ion sieve adsorbents also increased.

The Li^+ adsorption potential of the investigated SDS@Ag-CaO was somewhat high compared to the previously reported magnetite–lithium–manganese oxides, whose Li^+ adsorption potential was 1.2 mg/g in seawater [68]. Along with this, the recorded Li^+ adsorption amount by the SDS@Ag-CaO nanocomposite was also higher compared to the adsorbent materials previously investigated in the literature (as summarized in Table 1).

Table 1. Comparative analysis related to the Li^+ adsorption performance of designed nanocomposites with the previously reported adsorbents.

| Adsorbents | Adsorption Capacity q_e (mg/g) | References |
|----------------------------|-------------------------------------|------------|
| SDS@Ag-CaO | 3.28 | This work |
| PVP@Ag-CaO | 2.99 | This work |
| M-HMO-2.5 | 1.2 | [68] |
| Zeolite X | 0.30 | [69] |
| Lithium—aluminum hydroxide | 0.60 | [70] |
| CAC2 | 0.95 | [71] |
| BAC-1 | 0.87 | [72] |
| K. marxianus | 2.88 | [73] |

3.4.2. Zeta Potential Analysis

The zeta potential is a physical factor used to quantify the surface charge of a material. Here, the zeta potential of selected samples of the CaO-NPs, Ag-CaO-NPs, PVP@Ag-CaO, and SDS@Ag-CaO nanocomposites was determined at pH 10 to identify the strength of the negative charge density over the adsorbent surface. This negative charge strength most likely depends on the presence of negatively charged functional groups introduced by modification. Based on previously reported work, it was found that the modification of the adsorbent by chemicals containing anionic functional groups resulted in an increase in the negative value of the zeta potential compared to the original ones [74].

As shown in Figure 6a, the recorded zeta potentials of the PVP@Ag-CaO and SDS@Ag-CaO nanocomposites were -36.5 mV and -44.3 mV, respectively. It was found that the surface charge and negative zeta potential value of the SDS@Ag-CaO nanocomposites were very high because the surface was modified with an anionic surfactant (SDS). Based on previously reported literature, the particles functionalized with ionic surfactants had higher zeta potential values because the ionic surfactants increased the electrostatic repulsion between the particles and, thus, improved the physical stability [75]. On the other hand, a lower zeta potential value was recorded for PVP@Ag-CaO because PVP is a type of non-ionic surfactant. Typically, the non-ionic surfactant relies heavily on the steric hindrance effect to achieve the dispersion. However, if the zeta potential of the dispersion is lower, it can maintain an efficient degree of stability and decrease the aggregation of the particles [76,77].

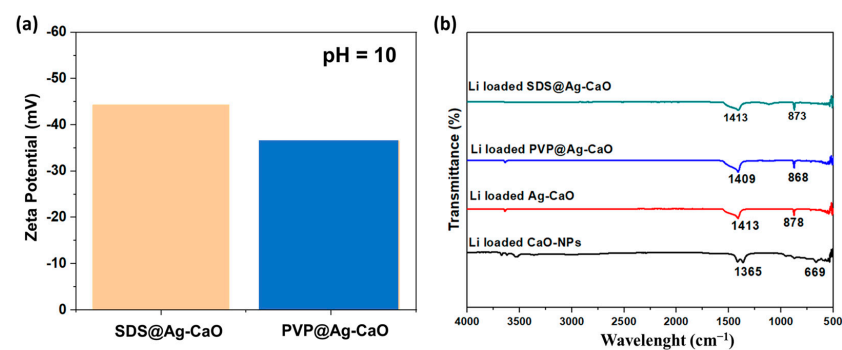


Figure 6. (a) Zeta potential of nanocomposites SDS@Ag-CaO and PVP@Ag-CaO at specified pH 10 and (b) FTIR spectra of Li^+ -loaded CaO-NPs, Ag-CaO-NPs, PVP@Ag-CaO, and SDS@Ag-CaO nanocomposites.

3.4.3. Li⁺ Adsorption Mechanism

The proposed Li⁺ adsorption mechanism of the nanocomposites is summarized in Figure 7a,b at low and high pH. It was observed that, at a low pH (between 2 to 4), there was a lower Li⁺ adsorption potential of all the nanocomposites; this might occur because, under an acidic condition, the greater number of positively charged hydrogen ions (H⁺) within the aqueous sources were attracted by the negatively charged $-SO_3^-$ group above the nanocomposite surface. This resulted in the protonation of most of the active functional groups; therefore, the Li⁺ ions were repelled by the positively charged surface of SDS@Ag-CaO due to repulsive forces (as mentioned in Figure 7a). Moreover, under a basic condition (at pH 10), no protonation occurred, and the negative charge density of the surface of SDS@Ag-CaO increased more, while the Li⁺ ions were adsorbed due to electrostatic attraction forces (Figure 7b). Therefore, the large number of Li⁺ ions in the aqueous source was strongly attracted to the surface of the negatively charged SDS@Ag-CaO by electrostatic attractive forces [78,79]. Further confirmation of the successful Li⁺ adsorption on the surface of the adsorbent was obtained by analyzing the FTIR spectra after performing the Li⁺ adsorption experiment. The FTIR spectra of the Li-loaded samples showed the disappearance and positional shift of several peaks, which could confirm the successful loading of Li⁺ on the active functional groups (Figure 6b).

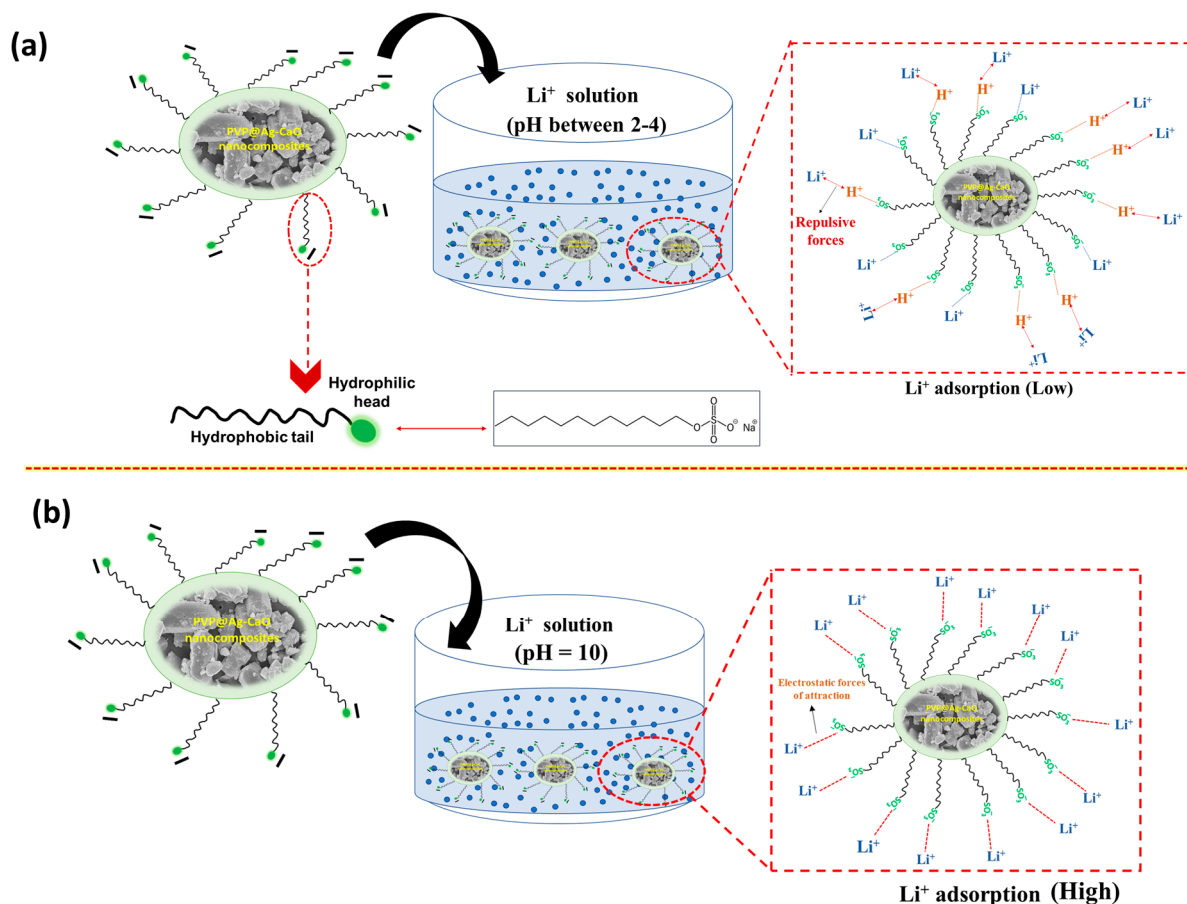


Figure 7. Proposed Li⁺ adsorption mechanism by SDS@Ag-CaO nanocomposite (a) under acidic condition (low pH) and (b) under basic condition (high pH).

3.5. Effect of Contact Time and Kinetic Analysis

Contact time is also an essential factor influencing the Li⁺ uptake potential of nanocomposites. To determine the equilibrium contact time, the Li⁺ adsorption performance of the SDS@Ag-CaO and PVP@Ag-CaO nanocomposites was carried out at different contact time durations (3, 4, 5, 8, and 10). A 0.1 g dosage of nanocomposites was added to 2 mg L⁻¹ of

Li^+ solution (optimized pH: 10) at ambient temperature. As shown in Figure 8a,b, in the initial stage, the rapid increase of the Li^+ adsorption potential of the nanocomposites was observed by increasing the time limit up to 8 h, because at the beginning, there was a high availability of an excessive number of active functional groups on the surface [80]. Once the equilibrium was achieved at the contact time interval of 8 h, no further increment in Li^+ uptake was noticed up to 10 h. As displayed in Figure 8a,b, the maximum recorded Li^+ uptake of the SDS@Ag-CaO and PVP@Ag-CaO nanocomposites at the equilibrium time (q_t) was increased to 3.28 mg/g and 2.99 mg/g with an Li^+ removal of 94.8% and 86.5%, respectively.

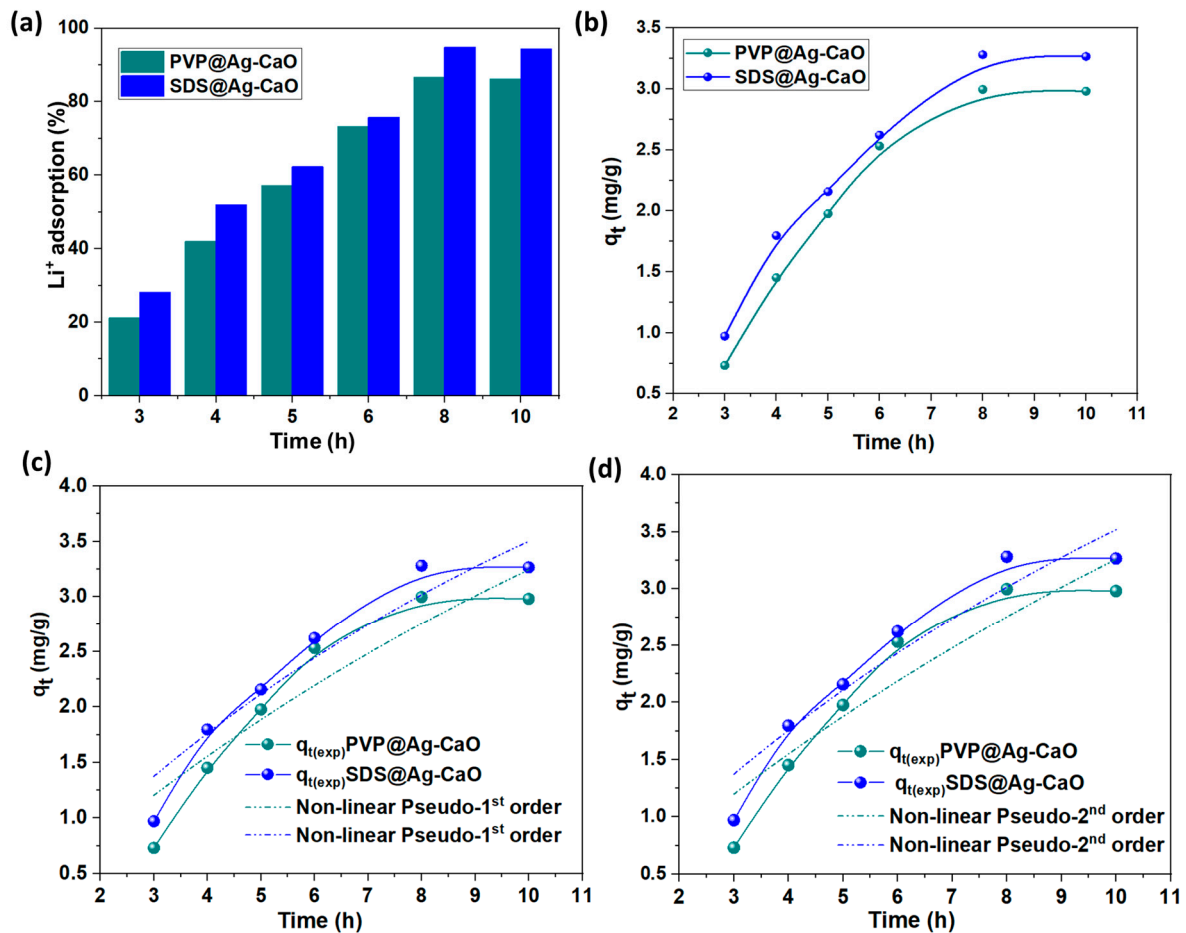


Figure 8. (a) Li^+ removal percentage at different contact time intervals, (b) Li^+ adsorption capacities at different contact time intervals, and non-linear kinetics plots of (c) pseudo-first-order model and (d) pseudo-second-order model of Li^+ uptake by PVP@Ag-CaO and SDS@Ag-CaO nanocomposites.

To examine the mechanism of Li^+ adsorption by the developed nanocomposites, two distinct kinetics models, namely pseudo-first-order and pseudo-second-order, were employed to analyze the adsorption data. The adsorption mechanistic phenomenon was established as physisorption if the experimental data followed pseudo-first-order kinetics. The non-linear kinetic expression of the pseudo-first-order model is given by Equation (4) [81]:

$$q_t = q_e \left(1 - e^{-k_1 t} \right) \quad (4)$$

The parameter denoted as k_1 represents the rate constant in this model. “ t ” is time.

The pseudo-second-order reaction rate is contingent upon the quantity of adsorption occurring in the solid phase. This reaction is employed specifically when the adsorption

mechanism involved is chemisorption. The non-linear pseudo-second-order expression is given by Equation (5) [82]:

$$q_e = \frac{(k_2 q_e^2 \cdot t)}{(1 + k_2 q_e^2 \cdot t)} \quad (5)$$

k_2 represents the rate constant in the context of the pseudo-second-order model.

The non-linear kinetic plots of pseudo-first-order and pseudo-second-order models are given in Figure 8c,d. The determined correlation coefficient (R^2) and the k_1 and k_2 values of the nanocomposites by the non-linear kinetic models are summarized in Table 2.

Table 2. Non-linear kinetics parameters and constants for Li^+ uptake by designed nanocomposites.

| Non-Linear Kinetic Models | Nanocomposites | Parameters and Constants | | | |
|---------------------------|----------------|--|-------|---------------------|---------------------|
| Pseudo-first-order | | k_1 (h^{-1}) | R^2 | q_t (cal.) (mg/g) | q_t (exp.) (mg/g) |
| | PVP@Ag-CaO | 0.065 | 0.899 | 6.745 | 3.28 |
| | SDS@Ag-CaO | 0.084 | 0.929 | 6.125 | 2.99 |
| Pseudo-second-order | | k_2 ($\text{g}/\text{mg} \times \text{h}$) | R^2 | q_t (cal.) (mg/g) | q_t (exp.) (mg/g) |
| | PVP@Ag-CaO | 2.89×10^3 | 0.828 | 12.370 | 3.28 |
| | SDS@Ag-CaO | 4.61×10^3 | 0.906 | 10.676 | 2.99 |

In general, the experimental adsorption data seemed to be well fit when the recorded R^2 values were close to unity (1). As shown in Table 2, the R^2 values of the nanocomposites (SDS@Ag-CaO and PVP@Ag-CaO) obtained by the non-linear equation of the pseudo-first-order model were high (0.899 and 0.929) and closer to 1 than the R^2 values obtained by the non-linear pseudo-second-order kinetics. This result showed the good fit of the experimental data with the pseudo-first-order model and confirmed the physisorption nature of the Li^+ adsorption process. In addition to this, as stated in Table 2, the experimental Li^+ uptake value (q_t (exp.)) was closer to the calculated q_t value “ q_t (cal.)” obtained by the non-linear pseudo-first-order model in contrast to the q_t (cal.) value calculated by the non-linear pseudo-second-order model. This also provides further confirmation of the best fit of the pseudo-first-order model.

3.6. Influence of Li^+ Initial Concentration and Isothermal Analysis

The influence of primarily the Li^+ concentration was also considered one of the important parameters that affected the adsorption potential of the nanocomposites. The experiment was performed by utilizing 0.1 g of samples within different concentrations of solutions of Li^+ (1, 2, 3, 4, and 5 mg L^{-1}) under optimized conditions (pH: 10, contact time: 8 h). It was observed that the Li^+ removal percentage by the SDS@Ag-CaO and PVP@Ag-CaO nanocomposite declined by increasing the initial Li^+ concentration up to 2 mg L^{-1} . However, the q_e value increased by increasing the initial Li^+ concentration up to 4 mg L^{-1} . The adsorption equilibrium was attained at 4 mg L^{-1} , because, with a further increase in the adsorbate concentration (5 mg L^{-1}), the Li^+ uptake potential remained constant. This scenario might occur because similar active functional sites above the nanocomposite surfaces were accessible for the rising Li^+ concentration, hence the resultant excessive loading of the functional active sites on the nanocomposites. The optimal initial Li^+ concentration was 2 mg L^{-1} because the highest Li^+ removal percentage was recorded.

Equilibrium isotherms were used to identify the linkage of the concentration of Li^+ ions adsorbed per unit weight of adsorbent and the Li^+ concentration left in the solution at equilibrium. Herein, two different isothermal models were used including Langmuir and Freundlich to determine the Li^+ adsorption behavior.

The Langmuir model illustrated that the adsorption behavior followed mono-layer formation over the homogenous surface [83]. The non-linear equation of this model is written as follows (Equation (6)).

$$q_e = \frac{(Q_{max}K_L \cdot C_e)}{(1 + K_L C_e)} \tag{6}$$

where C_e denotes the Li^+ concentration after attaining equilibrium. Q_{max} (mg/g) is the maximum adsorption concentration of the nanocomposites, and K_L is the Langmuir constant ($L\ mg^{-1}$).

In the Freundlich isotherm, the adsorption process is believed follow the forming of multiple layers over the heterogenous surface of the sample [84]. The non-linear form of this model is given by Equation (7).

$$q_e = K_F C_e^{1/n} \tag{7}$$

where k_F ($L\ mg^{-1}$) and “n” are a constant and a heterogeneity parameter, respectively.

The parameters and constants of the non-linear Langmuir and Freundlich models were calculated (summarized in Table 3). All the plotted non-linear isothermal graphs are illustrated in Figure 9a,b.

Table 3. Non-linear isothermal parameters and constants for Li^+ uptake by nanocomposites.

| Non-Isothermal Models | Nanocomposites | Parameters and Constants | | | |
|-----------------------|----------------|--------------------------|-------|------------------|---------------------|
| Langmuir | | K_L ($L\ mg^{-1}$) | R^2 | q_{max} (mg/g) | q_e (exp.) (mg/g) |
| | PVP@Ag-CaO | 2.356 | 0.910 | 6.438 | 3.28 |
| | SDS@Ag-CaO | 7.788 | 0.963 | 5.665 | 2.99 |
| Freundlich | | K_F ($L\ mg^{-1}$) | R^2 | n | |
| | PVP@Ag-CaO | 4.294 | 0.811 | 2.536 | |
| | SDS@Ag-CaO | 4.892 | 0.834 | 3.732 | |

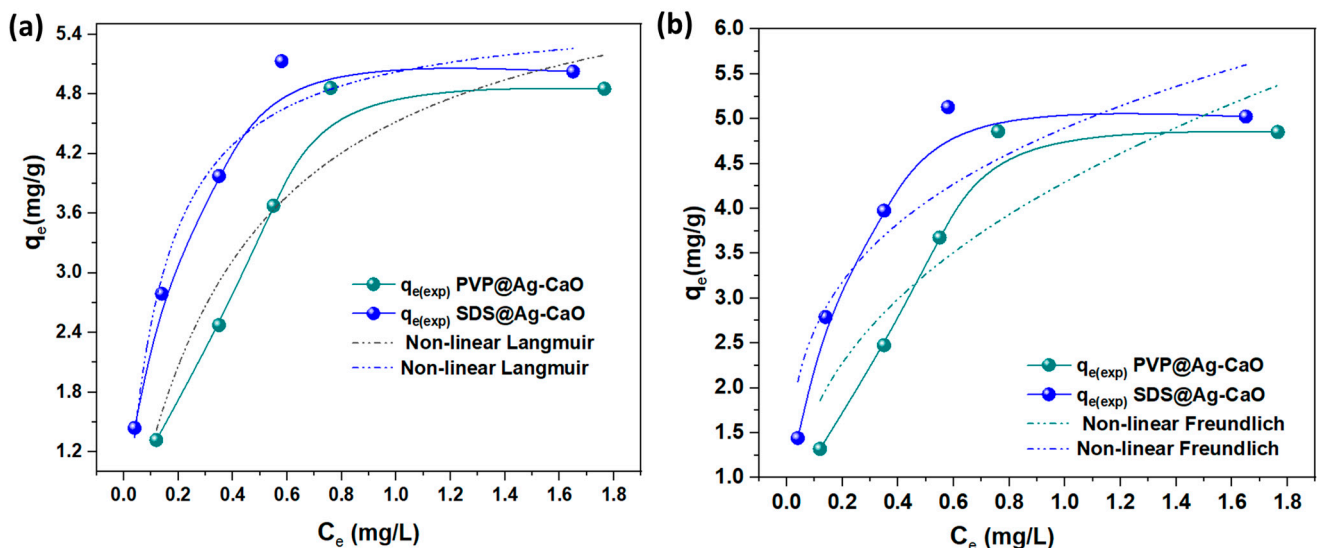


Figure 9. (a) Non-linear Langmuir isotherms and (b) non-linear Freundlich isotherms for Li^+ uptake by PVP@Ag-CaO and SDS@Ag-CaO nanocomposites.

Based on the parameters that were obtained by the non-linear equations of the Langmuir and Freundlich models (summarized in Table 3), the highest R^2 value was attained by the Langmuir model compared to the Freundlich model. This means that the Li^+ up-

take proceeded from the monolayer formation on the surfaces of the SDS@Ag-CaO and PVP@Ag-CaO nanocomposites.

3.7. Li^+ Recovery Examination by Desorption Experiment

The selection of a desorbing agent to achieve high metal recovery from materials is one of the most-important factors to be considered [17]. Based on the literature, it has been observed that the use of hydrochloric acid (HCl) as an eluting agent seems to be a very effective desorbing agent compared to other eluting agents such as nitric acid, acetic acid, ethanol, etc. [85]. The adsorbents were dried after performing batch adsorption experiments and were considered as Li-loaded samples. This Li^+ was recovered from these Li-loaded samples by using a HCl solution of different concentrations as the eluting agent (0.05, 0.5, and 1 M). By using Equation (3), the Li^+ desorption potential of the samples was calculated, and the obtained results are summarized in Figure 10. It was shown that, by increasing the concentration of the eluting agent (HCl) from 0.05 M to 1 M, the Li^+ desorption increased with values of 20–43%, 55–61%, 65–91%, and 58–85% for the CaO-NPs, Ag-CaO-NPs, PVP@Ag-CaO, and SDS@Ag-CaO, respectively. The desorption process was assumed to replace the adsorbed Li^+ ions above the adsorbent surface with the existing H^+ ions in the solution [86]. In addition, the increased electrostatic attractive forces within the H^+ ions and the active functional site may have facilitated the desorption phenomena. At a higher eluent concentration (1 M), the excess amount of H^+ ions within the aqueous source increased the ion exchange potential within the H^+ ions and sorbed the Li^+ ions from the adsorbent surface [19]. Therefore, the SDS@Ag-CaO nanocomposite exhibited an efficient Li^+ recovery ability from the aqueous source (91%), which can be considered as a potential candidate for enhanced Li^+ recovery application on an industrial scale.

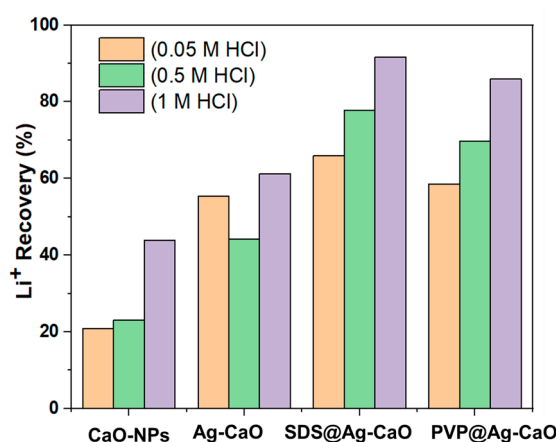


Figure 10. Li^+ desorption potential of the as-designed materials attained using HCl as an eluting agent under different concentrations.

The desorption potential usually reveals the ability of designed nanocomposites to undergo reutilization. It showed that the nanocomposites can be reused several times after desorption with an HCl eluting agent. This was evident from the previously reported work [87], which showed that hybrid nanocomposites can be reused within three consecutive Li adsorption–desorption cycles by utilizing HCl as a desorbing agent. Similarly, in other reported work, the designed adsorbent was regenerated and recycled five times after desorbing heavy metal (lead) ions by using HCl as an eluting agent [87].

4. Conclusions

In conclusion, pristine CaO-NPs, Ag-CaO-NPs, and surfactant-modified nanocomposites were synthesized by a simple chemical co-precipitation method. The surfactants used were SDS and PVP, which act as stabilizing and capping agents. The morphological, structural, crystallographic, and surface functional properties of the prepared materials

were investigated. Under optimum experimental conditions (pH (10), contact time (8 h), and initial Li^+ concentration (2 mg L^{-1})), the highest Li^+ adsorption efficiencies recorded by SDS@Ag-CaO and PVP@Ag-CaO were 3.28 mg/g and 2.99 mg/g , respectively. It was observed that surface modification with the SDS and PVP surfactants (acting as modifiers, stabilizers, and capping agents) significantly increased the Li^+ adsorption potential by increasing the number of negatively charged functional groups above the surface. Furthermore, the designed nanocomposites showed the potential to recover Li^+ ions from an aqueous source by using an eluting agent (HCl) with a concentration of 1 M. The SDS@Ag-CaO nanocomposite showed the highest Li^+ recovery potential (91%) as compared to the PVP@Ag-CaO (85%), Ag-CaO-NPs (61%), and CaO NPs (43%). Therefore, this invented stabilized nanocomposite is considered as a new adsorbent material for Li^+ recovery from aqueous sources and will motivate researchers to work on further improvement of such a type of material for efficient Li^+ recovery at an industrial scale. In addition, the identified innovative nanocomposite can also provide new insights and be considered for other potential applications such as lithium recovery from spent lithium ion batteries and direct lithium extraction/recovery from various aqueous sources.

Author Contributions: U.K.: conceptualization, investigation, methodology, validation, data curation, writing—original draft, writing—review and editing, supervision. H.J.: formal analysis, writing—review and editing. M.I.H.S.: funding acquisition. S.-J.P.: supervision, funding acquisition. All authors have read and agreed to the published version of the manuscript.

Funding: This research was supported by the National Research Foundation of Korea (NRF) grant funded by the Korea government (MSIT) (No. 2022M3J7A1062940).

Data Availability Statement: Not applicable.

Acknowledgments: The authors extend their appreciation to the Researchers Supporting Project Number (RSPD2023R999), King Saud University, Riyadh, Saudi Arabia.

Conflicts of Interest: The authors declare no conflict of interest.

References

1. Frith, J.T.; Lacey, M.J.; Ulissi, U. A non-academic perspective on the future of lithium-based batteries. *Nat. Commun.* **2023**, *14*, 420. [[CrossRef](#)] [[PubMed](#)]
2. Wu, L.; Liu, K.; Liu, J.; Pang, H. Evaluating the heat generation characteristics of cylindrical lithium-ion battery considering the discharge rates and N/P ratio. *J. Energy Storage* **2023**, *64*, 107182. [[CrossRef](#)]
3. Jamal, H.; Kang, B.S.; Lee, H.; Yu, J.S.; Lee, C.S. Comparative studies of electrochemical performance and characterization of TiO_2 /graphene nanocomposites as anode materials for Li-secondary batteries. *J. Ind. Eng. Chem.* **2018**, *64*, 151–166. [[CrossRef](#)]
4. Jamal, H.; Khan, F.; Lim, H.; Kim, J.H. Restraining lithium dendrite formation in all-solid-state Li-metal batteries via the surface modification of the ceramic filler. *Sustain. Mater. Technol.* **2023**, *35*, e00548. [[CrossRef](#)]
5. Jamal, H.; Khan, F.; Hyun, S.; Min, S.W.; Kim, J.H. Enhancement of the ionic conductivity of a composite polymer electrolyte via surface functionalization of SSZ-13 zeolite for all-solid-state Li-metal batteries. *J. Mater. Chem. A* **2020**, *9*, 4126–4137. [[CrossRef](#)]
6. Matalata, H.; Syafii, S.; Hamid, M.I. Evaluation of Future Battery Electric Vehicles as an Environmentally Friendly Transportation Means: A Review. *Andalasian Int. J. Appl. Sci. Eng.* **2023**, *3*, 32–43. [[CrossRef](#)]
7. Lee, C.S.; Jamal, H. Fabrication of TiO_2 Materials for Lithium-ion Batteries. *Lithium-Ion Batter. Mater. Appl.* **2020**, *80*, 1–27.
8. Cenci, M.P.; Scarazzato, T.; Munchen, D.D.; Dartora, P.C.; Veit, H.M.; Bernardes, A.M.; Dias, P.R. Eco-friendly electronics—A comprehensive review. *Adv. Mater. Technol.* **2022**, *7*, 2001263. [[CrossRef](#)]
9. Swain, B. Recovery and recycling of lithium: A review. *Sep. Purif. Technol.* **2017**, *172*, 388–403. [[CrossRef](#)]
10. Yang, S.; Zhang, F.; Ding, H.; He, P.; Zhou, H. Lithium metal extraction from seawater. *Joule* **2018**, *2*, 1648–1651. [[CrossRef](#)]
11. Dang, C.; Helal, A.S.; Zhu, L.; Xu, G.; Zhu, M. Industrial pathways to lithium extraction from seawater: Challenges and perspectives. *Nano Res. Eng.* **2023**, *2*, e9120059. [[CrossRef](#)]
12. Raiguel, S.; Nguyen, V.T.; Reis Rodrigues, I.; Deferm, C.; Riaño, S.; Binnemans, K. Recovery of lithium from simulated nanofiltration-treated seawater desalination brine using solvent extraction and selective precipitation. *Solvent Extr. Ion Exch.* **2023**, *41*, 425–448. [[CrossRef](#)]
13. Zhang, L.; Li, L.; Shi, D.; Peng, X.; Song, F.; Nie, F.; Han, W. Recovery of lithium from alkaline brine by solvent extraction with β -diketone. *Hydrometallurgy* **2018**, *175*, 35–42. [[CrossRef](#)]
14. Aljarrah, S.; Alsabbagh, A.; Almahasneh, M. Selective recovery of lithium from Dead Sea end brines using UBK10 ion exchange resin. *Can. J. Chem. Eng.* **2023**, *101*, 1185–1194. [[CrossRef](#)]

15. Sutijan, S.; Darma, S.A.; Hananto, C.M.; Sujoto, V.S.H.; Anggara, F.; Jenie, S.N.A.; Astuti, W.; Mufakhir, F.R.; Virdian, S.; Utama, A.P.; et al. Lithium separation from geothermal brine to develop critical energy resources using high-pressure nanofiltration technology: Characterization and optimization. *Membranes* **2023**, *13*, 86. [[CrossRef](#)]
16. Yu, H.; Hossain, S.M.; Wang, C.; Choo, Y.; Naidu, G.; Han, D.S.; Shon, H.K. Selective lithium extraction from diluted binary solutions using metal-organic frameworks (MOF)-based membrane capacitive deionization (MCDI). *Desalination* **2023**, *556*, 116569. [[CrossRef](#)]
17. Kamran, U.; Park, S.J. MnO₂-decorated biochar composites of coconut shell and rice husk: An efficient lithium ions adsorption-desorption performance in aqueous media. *Chemosphere* **2020**, *260*, 127500. [[CrossRef](#)]
18. Kamran, U.; Heo, Y.J.; Lee, J.W.; Park, S.J. Chemically modified activated carbon decorated with MnO₂ nanocomposites for improving lithium adsorption and recovery from aqueous media. *J. Alloys Compd.* **2019**, *794*, 425–434. [[CrossRef](#)]
19. Kamran, U.; Park, S.J. Hybrid biochar supported transition metal doped MnO₂ composites: Efficient contenders for lithium adsorption and recovery from aqueous solutions. *Desalination* **2022**, *522*, 115387. [[CrossRef](#)]
20. Fernández-Escalante, E.; Ibañez, R.; San-Román, M.F. Selective lithium separation from desalination concentrates via the synergy of extractant mixtures. *Desalination* **2023**, *556*, 116525. [[CrossRef](#)]
21. Kamran, U.; Park, S.J. Functionalized titanate nanotubes for efficient lithium adsorption and recovery from aqueous media. *J. Solid State Chem.* **2020**, *283*, 121157. [[CrossRef](#)]
22. Kamran, U.; Heo, Y.J.; Min, B.G.; In, I.; Park, S.J. Effect of nickel ion doping in MnO₂/reduced graphene oxide nanocomposites for lithium adsorption and recovery from aqueous media. *RSC Adv.* **2020**, *10*, 9245–9257. [[CrossRef](#)] [[PubMed](#)]
23. Park, H.; Singhal, N.; Jho, E.H. Lithium sorption properties of HMnO in seawater and wastewater. *Water Res.* **2015**, *87*, 320–327. [[CrossRef](#)] [[PubMed](#)]
24. Qian, F.; Guo, M.; Qian, Z.; Li, Q.; Wu, Z.; Liu, Z. Highly lithium adsorption capacities of H_{1.6}Mn_{1.6}O₄ ion-sieve by ordered array structure. *ChemistrySelect* **2019**, *4*, 10157–10163. [[CrossRef](#)]
25. Qian, F.; Zhao, B.; Guo, M.; Qian, Z.; Xu, N.; Wu, Z.; Liu, Z. Enhancing the Li⁺ adsorption and anti-dissolution properties of Li_{1.6}Mn_{1.6}O₄ with Fe, Co doped. *Hydrometallurgy* **2020**, *193*, 105291. [[CrossRef](#)]
26. Zandvakili, S.; Ranjbar, M. Preparation and characterisation of lithium ion exchange composite for the recovery of lithium from brine. *Min. Proc. Ext. Met. Rev.* **2018**, *127*, 176–181. [[CrossRef](#)]
27. Ameer, I.; Khantoul, A.R.; Boudine, B.; Brien, V.; Horwat, D.; Sebais, M.; Halimi, O. Effects of erbium incorporation on structural, surface Morphology, and degradation of methylene blue dye of magnesium oxide nanoparticles. *J. Inorg. Organomet. Polym. Mater.* **2023**, *33*, 30–46. [[CrossRef](#)]
28. Koçak, R.; Okcu, M.; Haliloğlu, K.; Türkoğlu, A.; Pour-Aboughadareh, A.; Jamshidi, B.; Janda, T.; Alaylı, A.; Nadaroğlu, H. Magnesium oxide nanoparticles: An influential element in Cowpea (*Vigna unguiculata* L. Walp) tissue culture. *Agronomy* **2023**, *13*, 1646. [[CrossRef](#)]
29. Naz, F.; Saeed, K. Synthesis of barium oxide nanoparticles and its novel application as a catalyst for the photodegradation of malachite green dye. *Appl. Water Sci.* **2022**, *12*, 121. [[CrossRef](#)]
30. Rani, M.; Keshu, U.; Shanker, U. Chicken eggshell waste derived calcium oxide based nanohybrid for rapid removal of heavy metal ions from water: Green synthesis, kinetics and reusability. *ChemistrySelect* **2023**, *8*, e202203540. [[CrossRef](#)]
31. Essien, U.I.; Odiongenyi, A.O.; Obadimu, C.O.; Enengedi, I.S. Investigation of snail shells as an adsorbent and precursor for the synthesis of calcium oxide nanoparticles for the removal of amoxicillin from aqueous solution. *Phys. Commun. Sci.* **2023**, *9*, 453–464.
32. Khine, E.E.; Koncz-Horvath, D.; Kristaly, F.; Ferenczi, T.; Karacs, G.; Baumli, P.; Kaptay, G. Synthesis and characterization of calcium oxide nanoparticles for CO₂ capture. *J. Nanopart. Res.* **2022**, *24*, 139. [[CrossRef](#)]
33. Zul, N.A.; Ganesan, S.; Hamidon, T.S.; Oh, W.D.; Hussin, M.H. A review on the utilization of calcium oxide as a base catalyst in biodiesel production. *J. Environ. Chem. Eng.* **2021**, *9*, 105741. [[CrossRef](#)]
34. Ahmad, W.; Kamboj, A.; Banerjee, I.; Jaiswal, K.K. Pomegranate peels mediated synthesis of calcium oxide (CaO) nanoparticles, characterization, and antimicrobial applications. *Inorg. Nano-Met.* **2022**, 1–8. [[CrossRef](#)]
35. Cherian, E.; Yazhini, D.; Victor, M.; Baskar, G. Production of biodiesel from pork fat using alumina-doped calcium oxide nanocomposite as heterogeneous catalyst. *Energy Sources Part A Recovery Util. Environ. Eff.* **2021**, *43*, 1386–1395. [[CrossRef](#)]
36. Thum, L.; Riedel, W.; Milojevic, N.; Guan, C.; Trunschke, A.; Dinse, K.P.; Risse, T.; Schomäcker, R.; Schlögl, R. Transition-metal-doping of CaO as Catalyst for the OCM reaction, a reality check. *Front. Chem.* **2022**, *10*, 768426. [[CrossRef](#)]
37. Suthakaran, S.; Dhanapandian, S.; Krishnakumar, N.; Ponpandian, N. Surfactants assisted SnO₂ nanoparticles synthesized by a hydrothermal approach and potential applications in water purification and energy conversion. *J. Mater. Sci. Mater. Electron.* **2019**, *30*, 13174–13190. [[CrossRef](#)]
38. Yang, J.; Shang, J.; Chen, J.; Xue, F.; Ke, Z.; Zhang, X.; Ding, E. Preparation and characterization of boron nitride nanosheet ferric oxide composite (BNNS@Fe₃O₄) through the double stabilization of PVP and its adsorption to Congo red. *J. Polym. Res.* **2021**, *28*, 71. [[CrossRef](#)]
39. Hong, J.; Xie, J.; Mirshahghassemi, S.; Lead, J. Metal (Cd, Cr, Ni, Pb) removal from environmentally relevant waters using polyvinylpyrrolidone-coated magnetite nanoparticles. *RSC Adv.* **2020**, *10*, 3266–3276. [[CrossRef](#)]

40. Huang, D.L.; Chen, G.M.; Zeng, G.M.; Xu, P.; Yan, M.; Lai, C.; Zhang, C.; Li, N.J.; Cheng, M.; He, X.X.; et al. Synthesis and application of modified zero-valent iron nanoparticles for removal of hexavalent chromium from wastewater. *Water Air Soil Pollut.* **2015**, *226*, 375. [[CrossRef](#)]
41. Ullah, S.; Hashmi, M.; Hussain, N.; Ullah, A.; Sarwar, M.N.; Saito, Y.; Kim, S.H.; Kim, I.S. Stabilized nanofibers of polyvinyl alcohol (PVA) crosslinked by unique method for efficient removal of heavy metal ions. *J. Water Process. Eng.* **2020**, *33*, 101111. [[CrossRef](#)]
42. Rezaei-Aghdam, E.; Shamel, A.; Khodadadi-Moghaddam, M.; Ebrahimzadeh-Rajaei, G.; Mohajeri, S. Synthesis of a nanocomposite containing CTAB-stabilized Fe₃O₄ magnetic nanoparticles and a comparison between the adsorption behavior of cobalt ions on the nanocomposite and *Typha latifolia* L. *Theor. Found. Chem. Eng.* **2022**, *56*, 131–140. [[CrossRef](#)]
43. Wang, S.; Zhong, D.; Xu, Y.; Zhong, N. Polyethylene glycol-stabilized bimetallic nickel–zero valent iron nanoparticles for efficient removal of Cr (VI). *New J. Chem.* **2021**, *45*, 13969–13978. [[CrossRef](#)]
44. Koczkur, K.M.; Mourdikoudis, S.; Polavarapu, L.; Skrabalak, S.E. Polyvinylpyrrolidone (PVP) in nanoparticle synthesis. *Dalton Trans.* **2015**, *44*, 17883–17905. [[CrossRef](#)]
45. Guzman, M.; Arcos, M.; Dille, J.; Rouse, C.; Godet, S.; Malet, L. Effect of the concentration and the type of dispersant on the synthesis of copper oxide nanoparticles and their potential antimicrobial applications. *ACS Omega* **2021**, *6*, 18576–18590. [[CrossRef](#)]
46. Si, R.; Zhang, Y.W.; You, L.P.; Yan, C.H. Self-organized monolayer of nanosized ceria colloids stabilized by poly (vinylpyrrolidone). *J. Phys. Chem. B* **2006**, *110*, 5994–6000. [[CrossRef](#)]
47. Mirghiasi, Z.; Bakhtiari, F.; Darezereshki, E.; Esmaeilzadeh, E. Preparation and characterization of CaO nanoparticles from Ca(OH)₂ by direct thermal decomposition method. *J. Ind. Eng. Chem.* **2014**, *20*, 113–117. [[CrossRef](#)]
48. Gnanaprakasam, A.; Sivakumar, V.M.; Thirumarimurugan, M. A study on Cu and Ag doped ZnO nanoparticles for the photocatalytic degradation of brilliant green dye: Synthesis and characterization. *Water Sci. Technol.* **2016**, *74*, 1426–1435. [[CrossRef](#)]
49. Kakarndee, S.; Nanan, S. SDS capped and PVA capped ZnO nanostructures with high photocatalytic performance toward photodegradation of reactive red (RR141) azo dye. *J. Environ. Chem. Eng.* **2018**, *6*, 74–94. [[CrossRef](#)]
50. Yu, C.; Shao, Z.; Hou, H. A functionalized metal-organic framework decorated with O–groups showing excellent performance for lead (II) removal from aqueous solution. *Chem. Sci.* **2017**, *8*, 7611–7619. [[CrossRef](#)]
51. Yan, J.; Li, R. Simple and low-cost production of magnetite/graphene nanocomposites for heavy metal ions adsorption. *Sci. Total Environ.* **2022**, *813*, 152604. [[CrossRef](#)]
52. Junior, A.C.G.; Coelho, G.F.; Schwantes, D.; Rech, A.L.; Campagnolo, M.Â.; Miola, A.J. Biosorption of Cu (II) and Zn (II) with açai endocarp *Euterpe oleracea* M. in contaminated aqueous solution. *Acta Sci. Technol.* **2016**, *38*, 361–370. [[CrossRef](#)]
53. Sharma, M.; Kumar, S.; Pandey, O.P. Photophysical and morphological studies of organically passivated core-shell ZnS nanoparticles. *Dig. J. Nanomater. Biostruct.* **2008**, *3*, 189–197.
54. Naeem, M.A.; Armutlulu, A.; Imtiaz, Q.; Donat, F.; Schäublin, R.; Kierzkowska, A.; Müller, C.R. Optimization of the structural characteristics of CaO and its effective stabilization yield high-capacity CO₂ sorbents. *Nat. Commun.* **2018**, *9*, 2408. [[CrossRef](#)] [[PubMed](#)]
55. Shalbahar, M.; Esmaeilzadeh, F.; Vakili-Nezhaad, G.R. Enhanced oil recovery by wettability alteration using iron oxide nanoparticles covered with PVP or SDS. *Colloids Surf. A Physicochem. Eng. Asp.* **2020**, *607*, 125509. [[CrossRef](#)]
56. Mohamed, F.; Shaban, M.; Aljohani, G.; Ahmed, A.M. Synthesis of novel eco-friendly CaO/C photocatalyst from coffee and eggshell wastes for dye degradation. *J. Mater. Res. Technol.* **2021**, *14*, 3140–3149. [[CrossRef](#)]
57. Jayabharathi, J.; Karunakaran, C.; Kalaiarasi, V.; Ramanathan, P. Nano ZnO, Cu-doped ZnO, and Ag-doped ZnO assisted generation of light from imidazole. *J. Photochem. Photobiol. A Chem.* **2014**, *295*, 1–10. [[CrossRef](#)]
58. Habte, L.; Shiferaw, N.; Mulatu, D.; Thenepalli, T.; Chilakala, R.; Ahn, J.W. Synthesis of nano-calcium oxide from waste eggshell by sol-gel method. *Sustainability* **2019**, *11*, 3196. [[CrossRef](#)]
59. Yadav, V.K.; Gnanamoorthy, G.; Yadav, K.K.; Ali, I.H.; Bagabas, A.A.; Choudhary, N.; Yadav, S.; Suriyaprabha, R.; Islam, S.; Modi, S.; et al. Utilization of incense stick ash in hydrometallurgy methods for extracting oxides of Fe, Al, Si, and Ca. *Materials* **2022**, *15*, 1879. [[CrossRef](#)]
60. Kotomin, E.A.; Popov, A.I. Radiation-induced point defects in simple oxides. *Nucl. Instrum. Methods Phys. Res. B* **1998**, *141*, 1–15. [[CrossRef](#)]
61. Chen, Q.; Yang, X.; Zhang, Y.; Nie, B.; Ding, Y. Influence of vacancy defects of the calcium oxide surface on the nonequilibrium phase transition of alkali metal salts. *Langmuir* **2022**, *38*, 818–827. [[CrossRef](#)] [[PubMed](#)]
62. Kumar, S.; Sharma, V.; Pradhan, J.K.; Sharma, S.K.; Singh, P.; Sharma, J.K. Structural, Optical and antibacterial response of CaO nanoparticles synthesized via direct precipitation technique. *Nano Biomed. Eng.* **2021**, *13*, 172–178. [[CrossRef](#)]
63. Imtiaz, A.; Farrukh, M.A.; Khaleeq-ur-Rahman, M.; Adnan, R. Micelle-assisted synthesis of Al₂O₃·CaO nanocatalyst: Optical properties and their applications in photodegradation of 2,4,6-trinitrophenol. *Sci. World J.* **2013**, *2013*, 641420. [[CrossRef](#)] [[PubMed](#)]
64. Samadianfard, R.; Seifzadeh, D.; Habibi-Yangjeh, A. Sol-gel coating filled with SDS-stabilized fullerene nanoparticles for active corrosion protection of the magnesium alloy. *Surf. Coat. Technol.* **2021**, *419*, 127292. [[CrossRef](#)]

65. Xiao, J.L.; Nie, X.Y.; Sun, S.Y.; Song, X.F.; Li, P.; Yu, J.G. Lithium ion adsorption–desorption properties on spinel $\text{Li}_4\text{Mn}_5\text{O}_{12}$ and pH-dependent ion-exchange model. *Adv. Powder Technol.* **2015**, *26*, 589–594. [[CrossRef](#)]
66. Al Najjar, T.; Allam, N.K.; El Sawy, E.N. Anionic/nonionic surfactants for controlled synthesis of highly concentrated sub-50 nm polystyrene spheres. *Nanoscale Adv.* **2021**, *3*, 5626–5635. [[CrossRef](#)]
67. Zheng, L.; Chen, J.; Sun, J.; Liu, M.; Gao, Y.; Guo, Z. Highly selective lanthanide-doped ion sieves for lithium recovery from aqueous solutions. *J. Chem. Res.* **2023**, *47*, 17475198231159051. [[CrossRef](#)]
68. Kim, J.; Oh, S.; Kwak, S.Y. Magnetically separable magnetite–lithium manganese oxide nanocomposites as reusable lithium adsorbents in aqueous lithium resources. *J. Chem. Eng.* **2015**, *281*, 541–548. [[CrossRef](#)]
69. Díez, E.; Redondo, C.; Gómez, J.M.; Miranda, R.; Rodríguez, A. Zeolite adsorbents for selective removal of Co (II) and Li (I) from aqueous solutions. *Water* **2023**, *15*, 270. [[CrossRef](#)]
70. Jiang, H.; Yang, Y.; Sun, S.; Yu, J. Adsorption of lithium ions on lithium-aluminum hydroxides: Equilibrium and kinetics. *Can. J. Chem. Eng.* **2020**, *98*, 544–555. [[CrossRef](#)]
71. Seron, A.; Benaddi, H.; Beguin, F.; Frackowiak, E.; Bretelle, J.L.; Thiry, M.C.; Badosz, T.J.; Jagiello, J.; Schwarz, J.A. Sorption and desorption of lithium ions from activated carbons. *Carbon* **1996**, *34*, 481–487. [[CrossRef](#)]
72. Jeong, J.M.; Rhee, K.Y.; Park, S.J. Effect of chemical treatments on lithium recovery process of activated carbons. *J. Ind. Eng. Chem.* **2015**, *27*, 329–333. [[CrossRef](#)]
73. Günan Yücel, H.; Aksu, Z.; Yalçinkaya, G.B.; Karatay, S.E.; Dönmez, G. A comparative investigation of lithium (I) biosorption properties of *Aspergillus versicolor* and *Kluyveromyces marxianus*. *Water Sci. Technol.* **2020**, *81*, 499–507. [[CrossRef](#)]
74. Shen, X.; Wang, J.; Xin, G. Effect of the zeta potential on the corrosion resistance of electroless nickel and PVDF composite layers using surfactants. *ACS Omega* **2021**, *6*, 33122–33129. [[CrossRef](#)] [[PubMed](#)]
75. Salihi, E.Ç.; Wang, J.; Coleman, D.J.; Šiller, L. Enhanced removal of nickel (II) ions from aqueous solutions by SDS-functionalized graphene oxide. *Sep. Sci. Technol.* **2016**, *51*, 1317–1327. [[CrossRef](#)] [[PubMed](#)]
76. Cortés, H.; Hernández-Parra, H.; Bernal-Chávez, S.A.; Prado-Audelo, M.L.D.; Caballero-Florán, I.H.; Borbolla-Jiménez, F.V.; González-Torres, M.; Magaña, J.J.; Leyva-Gómez, G. Non-ionic surfactants for stabilization of polymeric nanoparticles for biomedical uses. *Materials* **2021**, *14*, 3197. [[CrossRef](#)]
77. Vladislavjevic, G.T.; McClements, D.J. Modification of interfacial characteristics of monodisperse droplets produced using membrane emulsification by surfactant displacement and/or polyelectrolyte electrostatic deposition. *Colloids Surf. A Physicochem. Eng. Asp.* **2010**, *364*, 123–131. [[CrossRef](#)]
78. Ali, F.; Mehmood, S.; Ashraf, A.; Saleem, A.; Younas, U.; Ahmad, A.; Bhatti, M.P.; Eldesoky, G.E.; Aljuwayid, A.M.; Habila, M.A.; et al. Ag–Cu embedded SDS nanoparticles for efficient removal of toxic organic dyes from water medium. *Ind. Eng. Chem.* **2023**, *62*, 4765–4777. [[CrossRef](#)]
79. Çiçek, A.; Yılmaz, O.; Arar, O. Removal of lithium from water by aminomethylphosphonic acid containing resin. *J. Serbian Chem. Soc.* **2018**, *83*, 1059–1069. [[CrossRef](#)]
80. Staroń, P.; Chwastowski, J. Raphia-microorganism composite biosorbent for lead ion removal from aqueous solutions. *Materials* **2021**, *14*, 7482. [[CrossRef](#)]
81. Lagergren, S.Y. Zur Theorie der sogenannten, Adsorption geloster Stoffe, Kungliga Svenska Vetenskapsakad. *Handlingar* **1898**, *24*, 1–39.
82. Ho, Y.S.; McKay, G. Pseudo-second order model for sorption processes. *Process Biochem.* **1999**, *34*, 451–465. [[CrossRef](#)]
83. Langmuir, I. The adsorption of gases on plane surfaces of glass, mica and platinum. *J. Am. Chem. Soc.* **1918**, *40*, 1361–1403. [[CrossRef](#)]
84. Freundlich, H. Über die adsorption in losungen. (Adsorption in Solution). *Z. Phys. Chem.* **1906**, *57*, 385–470.
85. Zhang, X.; Hao, Y.; Chen, Z.; An, Y.; Zhang, W.; Wang, X. Lignocellulose@ activated clay nanocomposite with hierarchical nanostructure enhancing the removal of aqueous zn (II). *Polymers* **2019**, *11*, 1710. [[CrossRef](#)] [[PubMed](#)]
86. Sajab, M.S.; Chia, C.H.; Zakaria, S.; Sillanpää, M.I.K.A. Adsorption of heavy metal ions on surface of functionalized oil palm empty fruit bunch fibers: Single and binary systems. *Sains Malays.* **2017**, *46*, 157–165. [[CrossRef](#)]
87. Bayuo, J.; Abukari, M.A.; Pelig-Ba, K.B. Desorption of chromium (VI) and lead (II) ions and regeneration of the exhausted adsorbent. *Appl. Water Sci.* **2020**, *10*, 171. [[CrossRef](#)]

Disclaimer/Publisher’s Note: The statements, opinions and data contained in all publications are solely those of the individual author(s) and contributor(s) and not of MDPI and/or the editor(s). MDPI and/or the editor(s) disclaim responsibility for any injury to people or property resulting from any ideas, methods, instructions or products referred to in the content.